JOURNAL OF GEOPHYSICAL RESEARCH, VOL. 106, NO. D19, PAGES 22,965–22,977, OCTOBER 16, 2001

Surface variability effects on the remote sensing of thin cirrus optical and microphysical properties

P. Rolland and K. N. Liou

Department of Atmospheric Sciences, University of California, Los Angeles, California

Abstract. We have developed a methodology for the retrieval of the optical and microphysical properties of thin cirrus clouds with optical depths less than 0.5 using Moderate Imaging Spectroradiometer (MODIS) Airborne Simulator (MAS) measurements conducted during the Subsonic Aircraft Cloud and Contrail Special Study (SUCCESS). This methodology involves the use of correlated reflectance at three channels (0.65, 1.6, and 2.2 μm). We demonstrate the necessity of employing accurate values of the upwelling cloud base reflectance fields and present a method for the computation of these fields based on the atmospheric correction approach. For ocean surfaces the anisotropic reflectance is atmospherically corrected using appropriate radiative transfer calculations, along with the retrieved aerosol optical depths based on a simple aerosol microphysical model. For land surfaces a mosaic of ecosystems is used to compute the anisotropic reflectance associated with the surface terrain variability. We show that using these explicit computations of the emerging cloud base reflectance, thin cirrus optical depths and ice crystal size over ocean surfaces can be retrieved accurately. Uncertainties in the retrieved optical depth and ice crystal size are further reduced by 20 and 45%, respectively, over complex land surfaces.

1. Introduction

In a recent paper [*Rolland et al.*, 2000] we presented a methodology for the remote sensing of cirrus optical depth and ice crystal size utilizing reflectance measurements for three solar channels (0.65, 1.6, and 2.2 μm) available from the Moderate Imaging Spectroradiometer (MODIS) and MODIS Airborne Simulator (MAS). The retrieval method involved the construction of correlated bidirectional reflectance lookup tables for a number of cirrus optical depths and mean effective ice crystal sizes, based on light scattering and radiative transfer calculations. The single-scattering properties for representative ice crystals were determined from a unified theory for light scattering by ice crystals developed by *Liou et al.* [2000]. The adding-doubling method [*Takano and Liou,* 1989] was employed for radiative transfer calculations. The method simultaneously retrieves cirrus visible optical depth and mean effective ice crystal size in a three-dimensional correlated reflectance domain based on an optimal searching program. It was applied to MAS data in which a validation study was carried out.

Effects of the physical assumptions inherent to the technique were quantified and characterized in terms of the errors introduced in the retrieved quantities. We found that the retrieval of cirrus cloud parameters was extremely sensitive to the accuracy and precision of the cloud base bidirectional reflectance that is required in the construction of three-dimensional correlation lookup tables. The signal associated with the anisotropy of cloud base reflectance can be greater in magnitude than the total signal of thin cirrus with an optical depth lesser than ~0.5, particularly in the near-infrared (near-IR). In view of the significance of correcting thin cirrus effects for the retrieval of aerosols, greenhouse gases, and surface properties, it is the objective of this paper to develop a methodology to circumvent the errors associated with inaccurate cloud base reflectance.

In section 2, radiometric measurements of the thin cirrus over both ocean and complex land surfaces are used to illustrate the necessity of properly characterizing the cloud base emerging reflectance in conjunction with the retrieval method. In section 3, we introduce a methodology to calculate the emerging bidirectional reflectance at the cloud base for land and ocean surfaces. The variability of complex land surfaces is simulated using a 1-km resolution land cover database. Bidirectional reflectance distribution functions (BRDFs) are subsequently used to model the anisotropy of surface reflectance, while atmospheric correction is carried out based on explicit radiative transfer calculations that incorporate gaseous absorption and Rayleigh and aerosol scattering. In section 4, we present a number of case studies associated with radiometric measurements during Subsonic Aircraft Cloud and Contrail Special Study (SUCCESS) to illustrate the capability and limitation of the present remote sensing methodology for thin cirrus. Finally, conclusions are given in section 5.

2. Solar Retrieval Algorithm Limitation

The total observed radiance at the top of the atmosphere by an airborne or satellite sensor for a cirrus-filled pixel can be expressed by [*Liou*, 1980]

$$I(0;\mu,\phi) = I_c(0;\mu,\phi) + \frac{1}{\pi}\int_0^{2\pi}\int_0^1 T(\mu,\phi;\mu',\phi')I_s\mu' d\mu' d\phi' + I_s e^{-\tau/\mu} \tag{1}$$

where the last two terms represent, respectively, the diffuse and direct transmission of the upward isotropic radiance I_s; I_c is the cirrus radiance; and T is the transmission function

Paper number 2001JD900160.
0148-0227/01/2001JD900160$09.00

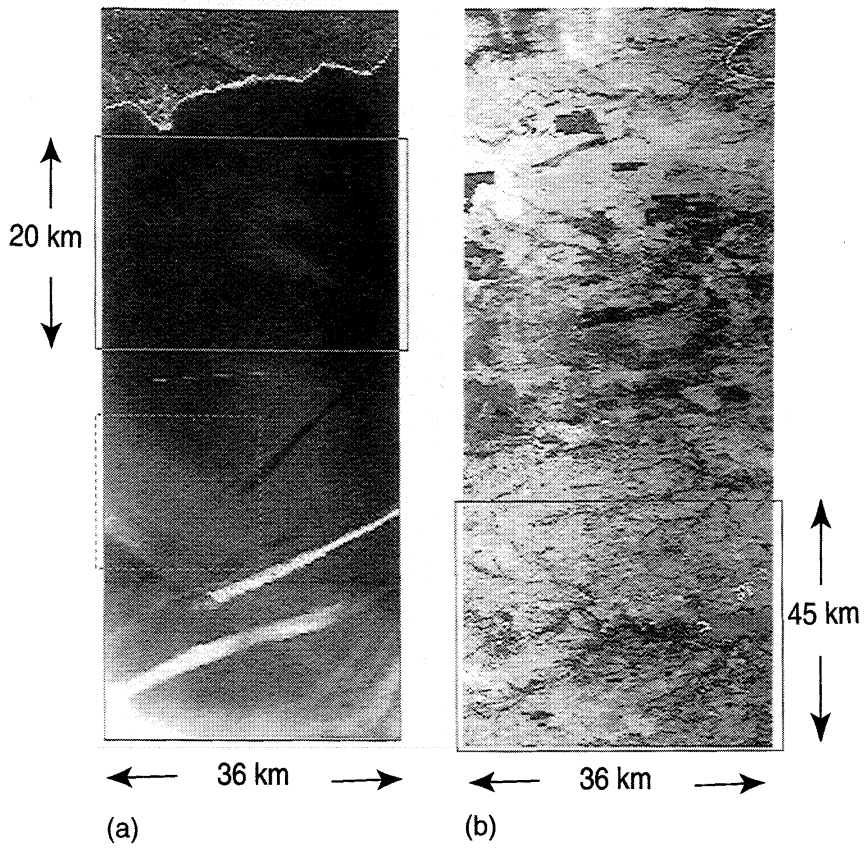

Figure 1. Visible (0.65-μm) imagery for the two MAS tracks used in this study. Figure 1a is an ocean background scene (May 12, 1996, 2220 to 2224 UTC). Figure 1b is a land background scene (April 20, 1996, 1641 to 1653 UTC). The solid boxes indicate cloud-free areas while the dashed box corresponds to a thin cirrus scene.

associated with the viewing geometry defined by the cosine of the solar zenith angle μ_0, the cosine of the radiometer scan zenith angle μ, and the relative azimuth angle $\Delta\phi$. Equation (1) can be rewritten in the form

$$I(0;\mu,\phi) = \mu_0 F_0 R_c(\mu_0,\mu,\Delta\phi) + I_s\gamma(\mu)\,, \qquad (2)$$

where the cloud bidirectional reflectance is defined by

$$R_c(\mu_0,\mu,\Delta\phi) = \frac{\pi I_c(0;\mu,\phi)}{\mu_0 F_0}\,, \qquad (3)$$

and the total directional transmittance is given by

$$\gamma(\mu) = e^{-\tau/\mu} + \frac{1}{\pi}\int_0^{2\pi}\int_0^1 T(\mu_0,\mu;\mu',\phi')\mu d\mu' d\phi'\,. \qquad (4)$$

Moreover, the reflected surface intensity can be expressed as

$$I_s = \frac{r_{cl}}{1-r_{cl}\alpha_c}\mu_0 F_0 \gamma(\mu_0)\,, \qquad (5)$$

where the emerging isotropic cloud base reflectance is

$$r_{cl} = \int_0^{2\pi}\int_0^1 r_s(\mu_0,\mu,\Delta\phi)d\mu d\phi \qquad (6)$$

and r_s is the surface bidirectional reflectance. Equation (2) can be expressed in terms of the observed bidirectional reflectance as follows:

$$R(\mu_0,\mu,\Delta\phi) = R_c(\mu_0,\mu,\Delta\phi) + \frac{\gamma(\mu_0)\gamma(\mu)r_{cl}}{1-r_{cl}\alpha_c}\,, \qquad (7)$$

where α_c is the cloud albedo (i.e., the hemispherical reflectance).

Equation (7) represents a typical parameterization equation that has been used to calculate theoretical bidirectional reflectance values for a combined surface/atmosphere/cirrus system, in which the cloud base reflectance is either obtained from clear pixel statistics [e.g., *Rolland et al.*, 2000; *Ou et al.*, 1993; *Arking and Childs*, 1985] or assumed to have a predetermined value [e.g., *Nakajima et al.*, 1991]. In both instances the upwelling cloud base radiance is assumed to be isotropic as well as invariable. While these approaches are satisfactory for the case of radiatively black clouds such as water clouds, large retrieval errors can occur in the case of more tenuous cirrus clouds. To illustrate this effect, we have selected two MAS tracks, as shown in Figure 1. Both scenes contain cloud-free and cirrus areas indicated by the superimposed solid and dashed rectangles, respectively. The ocean background scene was collected off the coast of California on May 12, 1996, while the land scene was observed over Kansas on April 20, 1996, both during SUCCESS. Representative values of the emerging cloud base reflectance were obtained from the histogram analysis of upwelling radiance measurements collected over cloud-free scenes for the 0.65, 1.6, and 2.2 μm channels. We calculate scene-averaged absolute spectral

Table 1. Scene-Averaged Absolute Differences Between the Observed Reflectances and Those Determined From Histogram Analysis

	0.65 μm	1.6 μm	2.2 μm
Ocean scene	0.0027	0.0031	0.0032
Land scene	0.0027	0.0031	0.0032

differences $\delta(\lambda)$ between the observed emerging reflectance for the three channels R_i, averaged at a 1 km spatial resolution and the three spectral reflectances determined from the histogram analysis, $R_{h,i}$, using the following relationship:

$$\delta(\lambda) = \frac{1}{N}\sum_{i=1}^{N}\left|R_i(\lambda,\mu_0,\mu,\Delta\phi) - R_{h,i}(\lambda)\right|, \qquad (8)$$

where N is the number of pixels in the clear scene. The results are given in Table 1. In Figure 2, we show theoretical values of the bidirectional reflectance for six mean effective ice crystal sizes ranging from 23 to 123 μm and for optical depths ranging from 0.1 to 2 using the average clear reflectance from which the spectral differences were added (solid lines) or subtracted (dashed lines). The calculations were conducted for the cases of ocean and land backgrounds. Errors introduced by incorrect values of the cloud base reflectance in the calculation of the combined emerging cloud top bidirectional reflectance can readily be seen to affect all the lookup table values. For the land background case, a significant shift is shown between two precomputed lookup tables. This shift is less noticeable for the ocean background case. In order to quantify this uncertainty in terms of the retrieved cloud parameters, sensitivity of the reflectance to these parameters is evaluated for a range of scattering angles (Θ) that are pertinent to the two MAS tracks selected. Displayed in Figure 3 is the visible reflectance sensitivity per unit optical depth ($\Delta R_{vis}/\Delta\tau$) for a range of mean effective ice crystal sizes corresponding to the microphysical models used in this study. Also shown is the near-IR reflectance sensitivity per unit mean effective ice crystal size ($\Delta R_{nir}/\Delta D_e$) for cirrus optical depths ranging from 0.1 to 8. These two parameters are calculated from the following relationships:

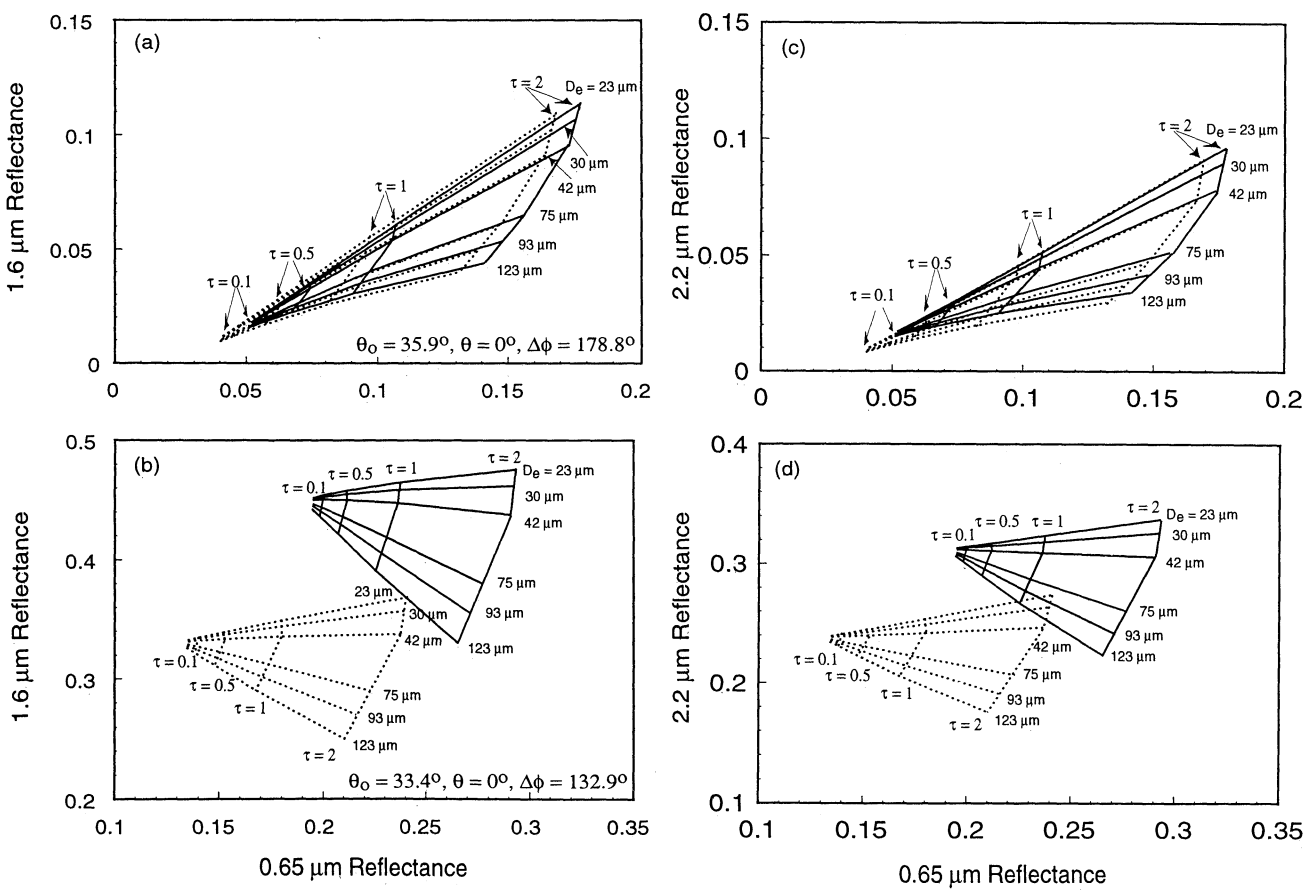

Figure 2. Correlation of the (a and b) 0.65- and 1.6-μm and (c and d) 2.2-μm bidirectional reflectances for a number of mean effective ice crystal sizes and optical depths. Calculations are presented for the emerging cloud base reflectance values obtained from the analysis of clear pixel histograms, plus (solid lines) or minus (dashed lines) one standard deviation. Figures 2a and 2c correspond to the ocean surface case (May 12, 1996). Figures 2b and 2d correspond to the land surface case (April 20, 1996).

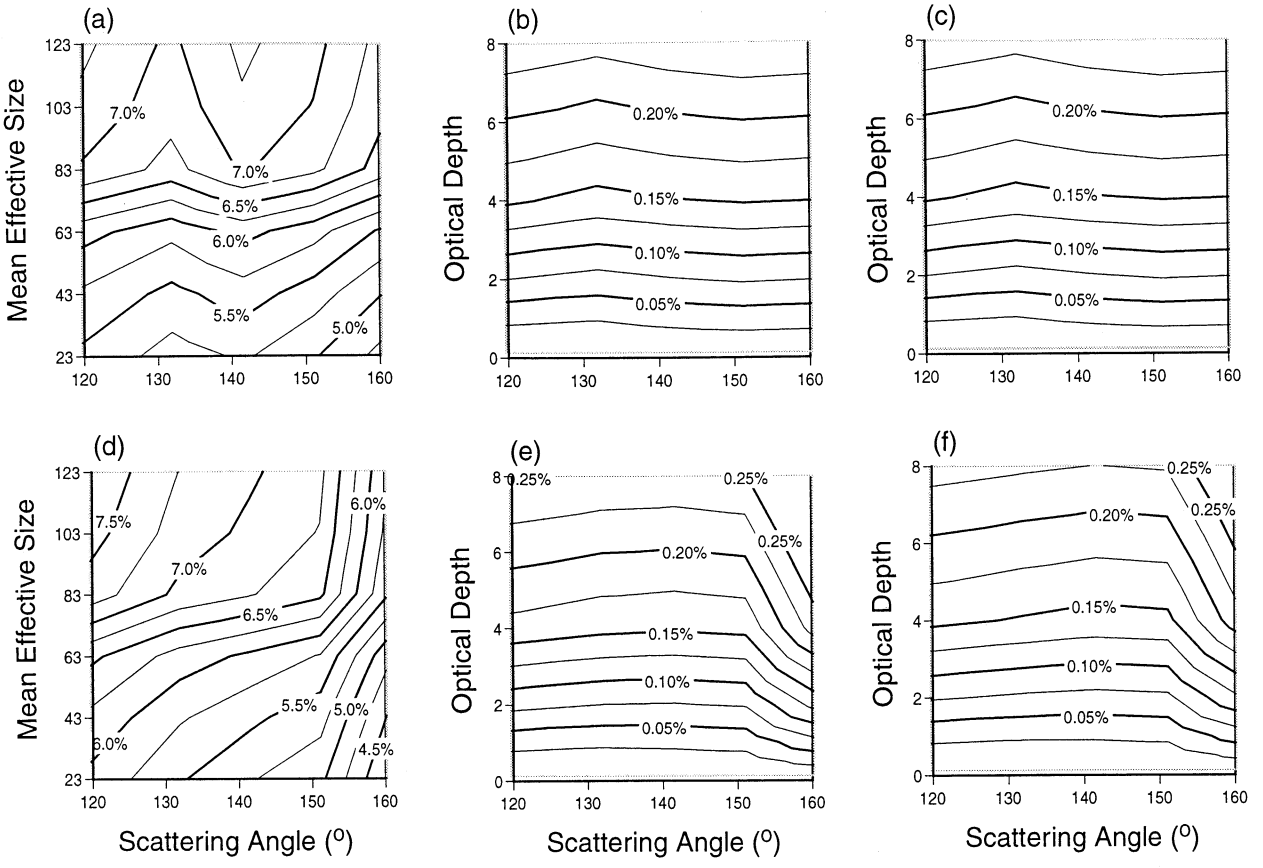

Figure 3. Spectral reflectance sensitivity for the MAS (a and d) 0.65-μm, (b and e) 1.6-μm, and (c and f) 2.2-μm channels. Panels a, b, and c are for the ocean scene, while panels d, e, and f are for the land scene. Visible sensitivity is given in percent reflectance per unit optical depth, near-infrared sensitivities are given in percent reflectance per unit size (1 μm). Results are shown for the scattering angles associated with the two scenes.

$$\frac{\Delta R_{vis}}{\Delta \tau} = \frac{1}{m}\sum_{i=1}^{m}\frac{R_{vis}(\tau_{i+1},\Theta,D_e)-R_{vis}(\tau_i,\Theta,D_e)}{\tau_{i+1}-\tau_i} = \sum_{n=0}^{3} a_n D_e^{\,n} \tag{9}$$

$$\frac{\Delta R_{nir}}{\Delta D_e} = \frac{1}{m}\frac{1}{n}\sum_{i=1}^{m}\sum_{j=1}^{n}\frac{R_{nir}(D_{e,i+1},\Theta_j,\tau)-R_{nir}(D_{e,i},\Theta_j,\tau)}{D_{e,i+1}-D_{e,i}} = \sum_{n=0}^{2} b_n \tau^n \tag{10}$$

where the parametric coefficients a_n and b_n are listed in Tables 2 and 3, respectively. Using (9) and (10) and the spectral reflectance differences defined in (8), uncertainty in the retrieved parameters can be evaluated. It can be seen from Figure 4 that uncertainty in the retrieved mean effective ice crystal size for the case involving the complex land surface is so large that an accurate retrieval of this parameter is not practical. As shown, it is not feasible to achieve an accuracy within 20 μm for cirrus optical depths smaller than ~4.5. Uncertainty in the retrieved optical depth ranges from ~0.35 to 0.65. For the ocean surface case, uncertainty in the retrieved optical depth is negligible. However, significant errors can be produced in the retrieved mean effective ice crystal size for thin cirrus. For instance, an error of 20 μm is seen for a cirrus optical depth of ~0.5. On the basis of the preceding analysis, it is clear that using single values (for the three channels) of the cloud base upwelling radiance *a priori* prevent the reliable retrieval of the values of the optical depth and ice crystal size for thin cirrus, particularly over complex land ecosystems.

The effects of instrument noise were also examined in terms of the error introduced on the retrieval results. The noise-equivalent radiance estimates presented by *King et al.* [1996] were employed. The data for the solar spectrum channels are based on MAS in-flight measurements over the Gulf of Mexico for low signal level, and clouds on the north slope of Alaska for high signal level. Linear interpolation between these two observations was employed to determine the noise-equivalent reflectance function for the two scenes used in the present study. Equations (9) and (10) were then used to evaluate the uncertainty introduced in the retrieved parameters by instrument noise. We found that this effect produces an optical depth uncertainty of ~0.01 and a mean effective ice crystal size uncertainty of 2 to 3 μm, much smaller than the uncertainties discussed in the present paper.

3. Simulation of the Cloud Base Upwelling Radiance

In order to alleviate the source of errors described in the previous section, we undertake an explicit modeling of the emerging bidirectional reflectance at the cloud base. The reflectance fields thus obtained (1 km resolution) are

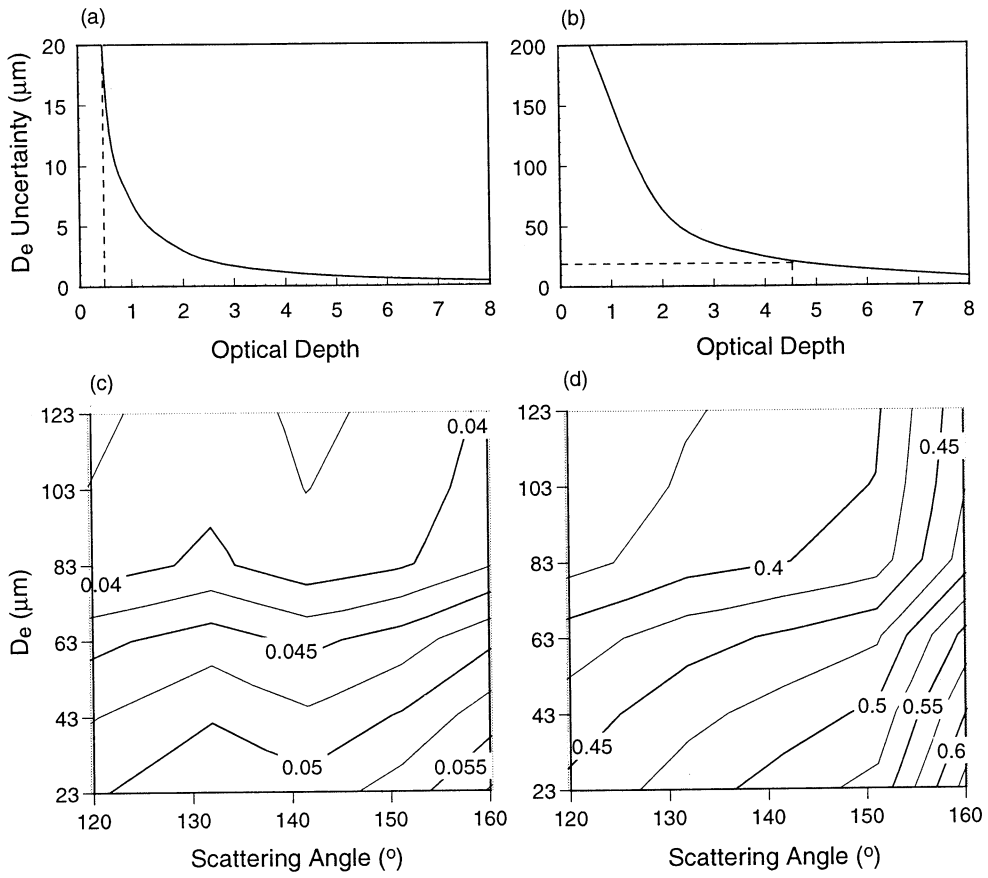

Figure 4. Uncertainties in the retrieved mean effective ice crystal size for the (a) ocean and (b) land scenes, shown as a function of the cirrus optical depth. Uncertainties in the retrieved cirrus optical depth for the (c) ocean and (d) land scenes, shown as a function of the cirrus mean effective ice crystal size and the scattering angle.

subsequently used in the calculation of lookup tables in conjunction with the cirrus retrieval algorithm.

3.1. Ocean Surfaces

The emerging cloud base reflectance over ocean surfaces is composed of sunlight backscattered by the surface and the atmospheric constituents, subsequently modified by absorption and scattering processes in the atmosphere. *Morel and Gentilli* [1993] have shown that backscattering of sunlight by ocean surfaces is not isotropic. In order to accurately simulate the emerging cloud base reflectance, the bidirectional characteristics of water-leaving reflectance must be properly accounted for. *Koepke* [1984] has illustrated that the spectral reflectance of an ocean surface (R_{oc}) is composed of three components: reflection due to white caps (R_{wc}), specular reflection (R_{sp}) including sunglint effects, and underlight (R_u). Thus we may write

$$R_{oc} = R_{wc} + (1-W)R_{sp} + (1-R_{wc})R_u\,, \qquad (11)$$

where W is the relative area covered by white caps. The white cap reflectance can be calculated using the reflectance model developed by *Koepke* [1984] in the form

$$R_{wc}(\lambda) = WR_{ef}(\lambda)\,, \qquad (12)$$

where R_{ef} is the effective ocean foam reflectance accounting for white caps specular characteristics as a function of age. The specular reflectance of ocean water can be calculated from the Fresnel formula using the refractive indices for water that correspond to typical ocean salinity and chlorinity. Further, the slopes of the waves can be determined from the analytic model developed by *Cox and Munk* [1954, 1955]. Finally, the reflectance due to underlight for ocean waters is effective only for the 0.65-μm channel and can be computed from the following relationship:

$$R_u(\mu_0,\mu,\Delta\phi) = \frac{1}{m^2}\frac{\omega(\lambda)\gamma_w(\mu_0)\gamma_w(\mu)}{1-a\omega(\lambda)}\,, \qquad (13)$$

where m is the index of refraction of ocean water, γ_w is the air-water interference directional transmittance, a is the diffuse attenuation coefficient of light in ocean water, and ω is the ratio of the upwelling to downwelling radiance just below the surface, which can be parameterized from the ratio of the sea water total absorption $A(\lambda)$ and backscattering $B(\lambda)$ coefficients [*Morel and Prieur,* 1977] in the form

$$\omega(\lambda) = 0.33\frac{B(\lambda)}{A(\lambda)}\,. \qquad (14)$$

Note that in this scheme, both the white cap reflectance and sun glint calculations are dependent on the surface wind speed and direction [*Cox and Munk,* 1955; *Koepke*, 1984].

The upwelling radiance over dark surfaces, such as the open ocean in the red and near-IR spectrum, mainly depends

Table 2. Parametric Coefficients for Equation (9)

	Θ, deg	a_0, $\times 10^{-2}$	a_1, $\times 10^{-4}$	a_2, $\times 10^{-5}$
Ocean	120	5.95	-4.44	1.10
	140	5.67	-3.89	1.10
	160	5.05	-3.84	1.08
Land	120	6.36	-4.10	1.03
	140	5.64	-3.58	0.97
	160	4.58	-3.16	0.85

on the type and concentration of atmospheric aerosol particles [*Stowe et al., 1997*]. Thus atmospheric correction for the spectral channels used in the present method is of utmost importance. Atmospheric correction of the emerging water-leaving reflectance was performed by accounting for Rayleigh scattering, gaseous absorption, and aerosol scattering and absorption using the modified Second Simulation of the Satellite Signal in the Solar Spectrum (6S) model developed by *Vermote et al.* [1997].

In order to accurately simulate the aerosol contribution, the aerosol optical depth was determined from the cloud-free scene by comparing the observed emerging reflectances at 0.74 and 0.86 μm with the computed clear sky reflectance (R_a), based on an oceanic aerosol model [*d'Almeida,* 1991]. Optimizing the probability that the measured reflectance $R(\mu_0, \mu, \Delta\phi)$ has the functional form $R_a(\tau_a, \mu_0, \mu, \Delta\phi)$ is equivalent to minimizing the following statistical formulation:

$$\chi^2 = \sum_i [\ln R_i(\mu_0, \mu, \Delta\phi) - \ln R_{a,i}(\tau_a, \mu_0, \mu, \Delta\phi)]^2 , \qquad (15)$$

where the summation extends over the two spectral channels, and τ_a is the assumed aerosol optical depth used in theoretical calculations. An aerosol optical depth can then be obtained from this minimization procedure. The selection of the two spectral channels (0.74 and 0.86 μm) for this retrieval is based on their near-zero water leaving reflectance [e.g., *Gordon and Wang, 1994*] and the availability of corresponding channels on MODIS. Once an aerosol optical depth is inferred for the cloud-free portion of the image, the same atmospheric conditions are assumed for the adjacent cirrus scene. The clear portion of the image can then be simulated at the three wavelengths that are used in the cirrus retrieval algorithm. Subsequently, the emerging cloud base bidirectional reflectance for the adjacent cirrus scene can be determined using appropriate sun/sensor geometry. The resulting bidirectional reflectance fields provide the cloud base reflectance values that are necessary to generate the lookup tables for the combined surface/atmosphere/cirrus reflectance based on (7). Thus, in the present technique, a set of the lookup tables is generated for each square kilometer of the MAS imagery. Using these tables in the retrieval algorithm leads to the decoupling of the combined surface/aerosol signal from the cirrus signal, thus allowing simultaneous retrieval of the cirrus parameters and aerosol optical depth.

3.2. Land Surfaces

The emerging cloud base reflectance over land surfaces is dominated by surface reflection processes. Thus, in order to simulate accurately the emerging cloud base reflectance, we must properly account for the land-leaving radiance. However, unlike open ocean surfaces, land ecosystems are often very inhomogeneous, resulting in both intrapixel variance and pixel-to-pixel variability. Furthermore, each type of land surface reflects light differently when viewed at different angles. For instance, the complex land scene presented in Figure 1 displays a range of emerging cloud-free reflectances of 4 to 24%, 2 to 54%, and 2 to 50% for the 0.65-, 1.6-, and 2.2-μm channels, respectively. Thus, accurate determination of the land-leaving radiance for complex land surfaces can be viewed as a two-step problem. First, the type of land surface for a given pixel must be established. Second, its anisotropic radiative signal must be correctly modeled in order to simulate reliably the spectral bidirectional reflectances for a given sun/sensor geometry.

For the present study the land cover for the selected MAS scenes was determined using the seasonal land cover/land use database developed by *Loveland et al.* [1995]. Monthly composited Advanced Very High Resolution Radiometer (AVHRR) local area coverage data for one year (April 1992 to March 1993) were used to generate a seasonal classification of land cover types for the continental United States. The resulting clusters were further stratified based on ancillary environment data such as elevation and ecoregion. The 205 class labels were assigned based on temporal curves of the clusters, as well as a large number of ancillary sources. The reliability of this data set is evidently being limited by the quality of the composited vegetation index data, as well as the accuracy of the ancillary sources. Nevertheless, it represents the most useful large area classification at a 1-km spatial resolution available at the time when SUCCESS was carried out [e.g., *Strahler and Townshend,* 1996].

Once the nature of the ecosystems present in a given scene is established, BRDFs can then be used to simulate the land-leaving radiance. For the present study, the BRDF calculations are based on a semiempirical, kernel-based modeling approach introduced by *Roujean et al.* [1992]. The underlying assumption of this type of models is the superposition of the surface and volume scattering components using an empirical coefficient (κ) characterizing their respective weights in the final bidirectional signature in the form

$$r_s(\mu_0, \mu, \Delta\phi) = \kappa r_{ss} + (1-\kappa) r_v , \qquad (16)$$

where r_{ss} and r_v are the surface and volume scattering reflectances, respectively. Mathematically, we may write

$$r_s(\mu_0, \mu, \Delta\phi) = f_i + f_v k_v(\mu_0, \mu, \Delta\phi) + f_s k_s(\mu_0, \mu, \Delta\phi) , \qquad (17)$$

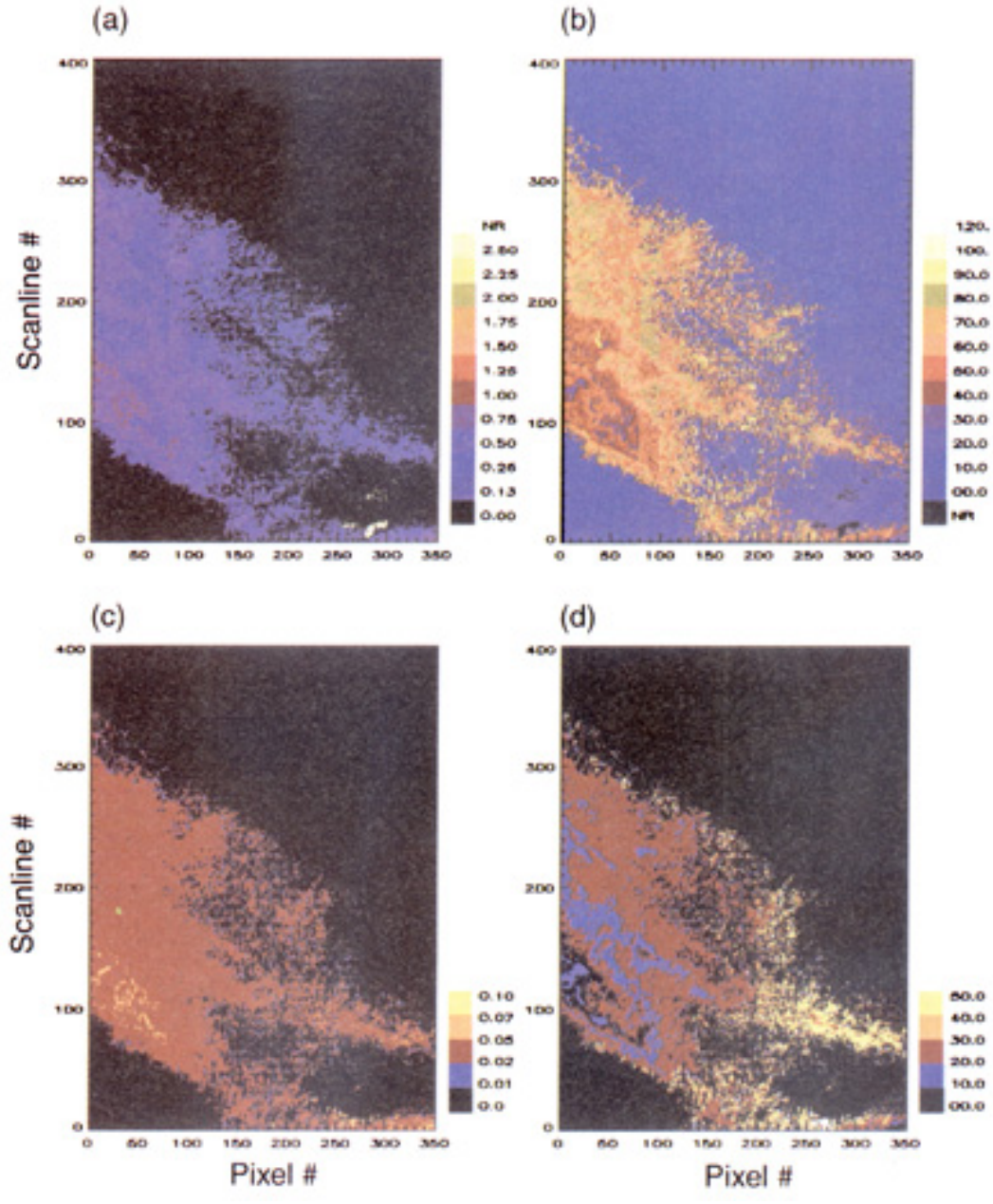

Plate 1. (a) Retrieved optical depth and (b) mean effective ice crystal size and (c and d) the associated uncertainties for the cirrus scene identified in Figure 1a.

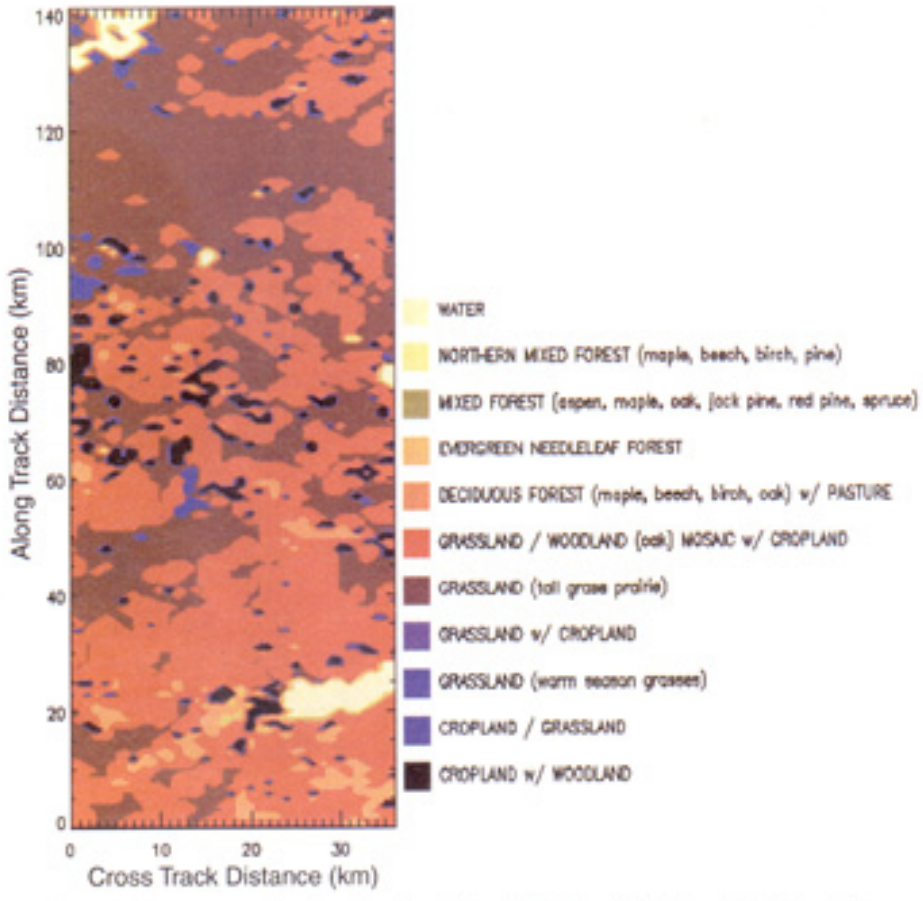

Plate 2. Ecosystem classification for the land MAS track displayed in Figure 1b.

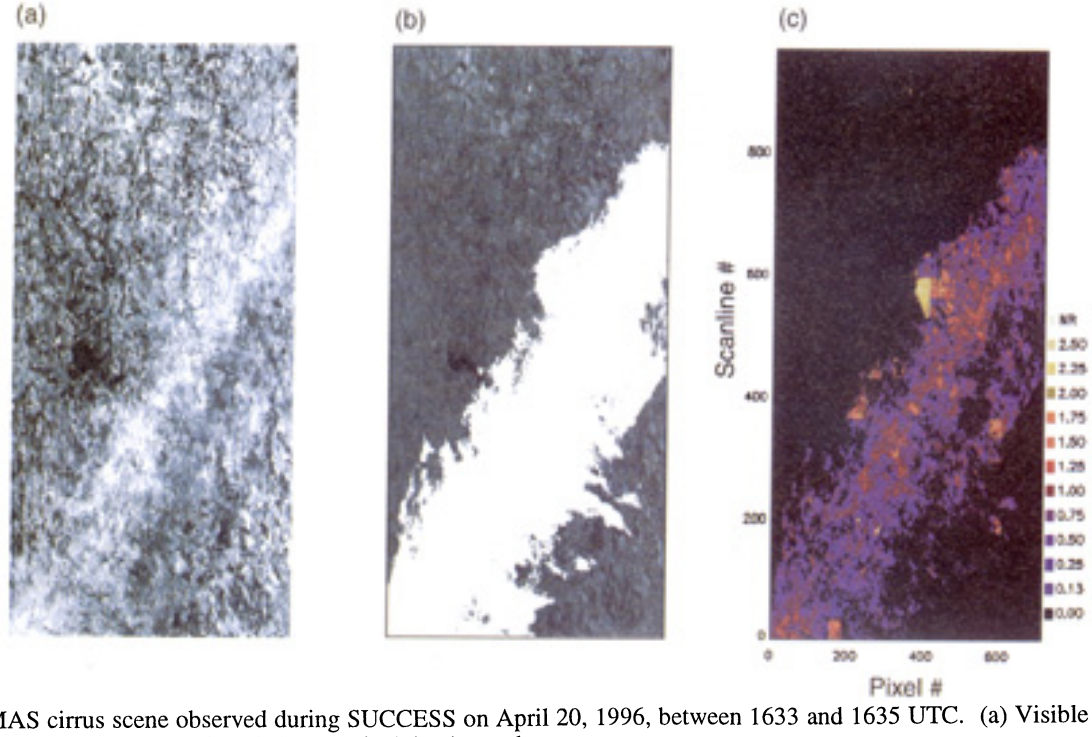

Plate 3. MAS cirrus scene observed during SUCCESS on April 20, 1996, between 1633 and 1635 UTC. (a) Visible imagery, (b) cloud mask, and (c) the retrieved cirrus optical depth are shown.

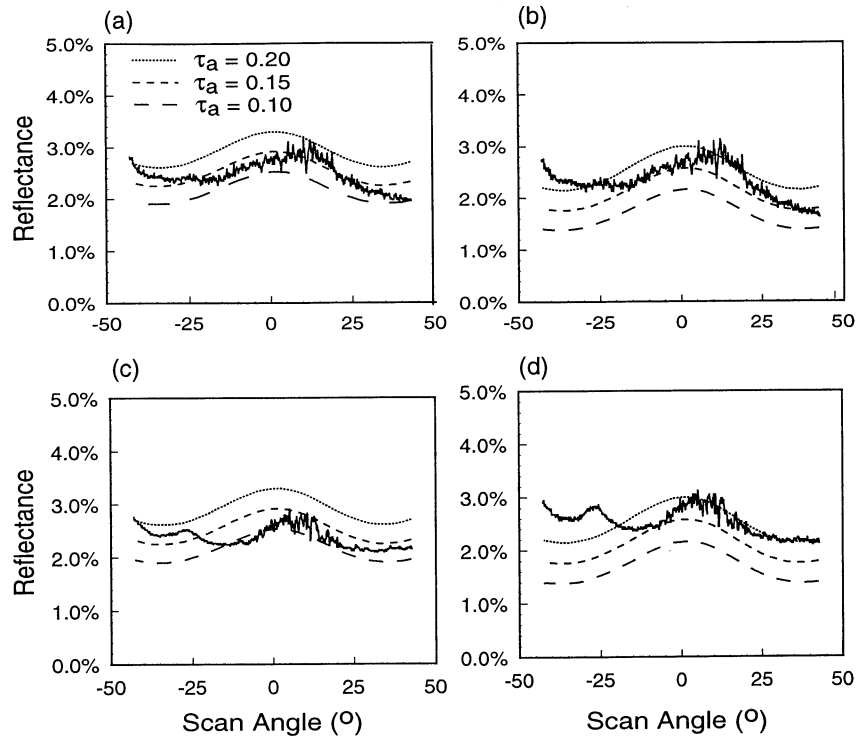

Figure 5. Observed spectral reflectance (solid lines) and corresponding theoretical calculations (dotted and dashed lines). Figures 5a and 5b correspond to the first scan line of the clear scene shown in Figure 1a, while Figures 5c and 5d correspond to the last scan line. Figures 5a and 5c are for the 0.74-μm channel, while Figures 5b and 5d are for the 0.86-μm channel.

where k_v and k_s are kernel functions, and f's are the weights of these functions. In (17), k_v and k_s are obtained from the geometric optics approximation, based on opaque vertical protrusions oriented at random and associated shadowing effects and homogeneous volumes of dispersed facets to represent the volume scattering in canopies. The kernel associated with the constant f_i is the isotropic Lambertian kernel which is unity. The weights of kernel functions are related to the physical properties of the modeled surface, and are based on *in situ* measurements obtained by *Kimes* [1983] and *Kimes et al.* [1985, 1986] in conjunction with leaf area index, soil albedo, and the average width and height of the protuberances. The model's linearity in terms of surface parameters makes it applicable to heterogeneous surfaces, thus allowing the treatment of pertinent ecosystems using mosaics of vegetation and soil types. Radiative transfer calculations for the atmospheric correction of land-leaving reflectance are then performed using the 6S model [*Vermote et al.*, 1997]. Once the clear portion of the image is reliably simulated at the three wavelengths that are used in the retrieval algorithm, the emerging cloud base reflectance for the adjacent cirrus scene can subsequently be determined.

4. Case Studies

4.1. Ocean Surfaces

On May 12, 1996, MAS was flown onboard the NASA ER-2 high-altitude research aircraft off the coast of northern California during the SUCCESS field campaign. The objective of this mission was to perform radiometric measurements of cirrus over uniform background water. For the present study, track 12 (shown in Figure 1a), which was collected between 2220 and 2224 UTC, was selected for its availability of adjacent thin cirrus (dashed rectangle) and cloud-free (solid rectangle) areas. Additionally, a nearby buoy (NOAA buoy 46030) provides concurrent wind speed and direction data, required for the calculation of water-leaving radiance.

Computations of the reflectance as a function of the sun/sensor geometry for the three channels used in the retrieval were carried out for 400 cloud-free MAS scan lines (716 pixels per scan line) according to the method described in subsection 3.1. In order to obtain the aerosol optical depth that is required for carrying out the atmospheric correction, theoretical calculations of the emerging clear sky reflectance were carried out for a number of assumed aerosol optical depths ranging from 0.05 to 0.25 until the best fit was obtained between observed and modeled fields for the two channels considered, using (15). This procedure is illustrated in Figure 5 where the observed spectral reflectance for the first and last lines of the clear scene shown in Figure 1a are displayed along with the corresponding theoretical calculations for aerosol optical depths ranging from 0.1 to 0.2. An aerosol optical depth of 0.17 provides the best fit for the scene selected. Reflectances for the three channels used in the cirrus retrieval were then calculated for the clear scene using the retrieved aerosol optical depth. Scene-averaged absolute values of the reflectance differences are 0.0020, 0.0026, and 0.0023 for the 0.6-, 1.6-, and 2.2-μm channels, respectively, which correspond to improvements in the relative accuracy of ~26% for the visible channel and 25% for the near-IR channels.

Once the clear portion of the image is satisfactorily simulated, the emerging cloud base bidirectional reflectances for the adjacent scan lines containing the thin cirrus targeted

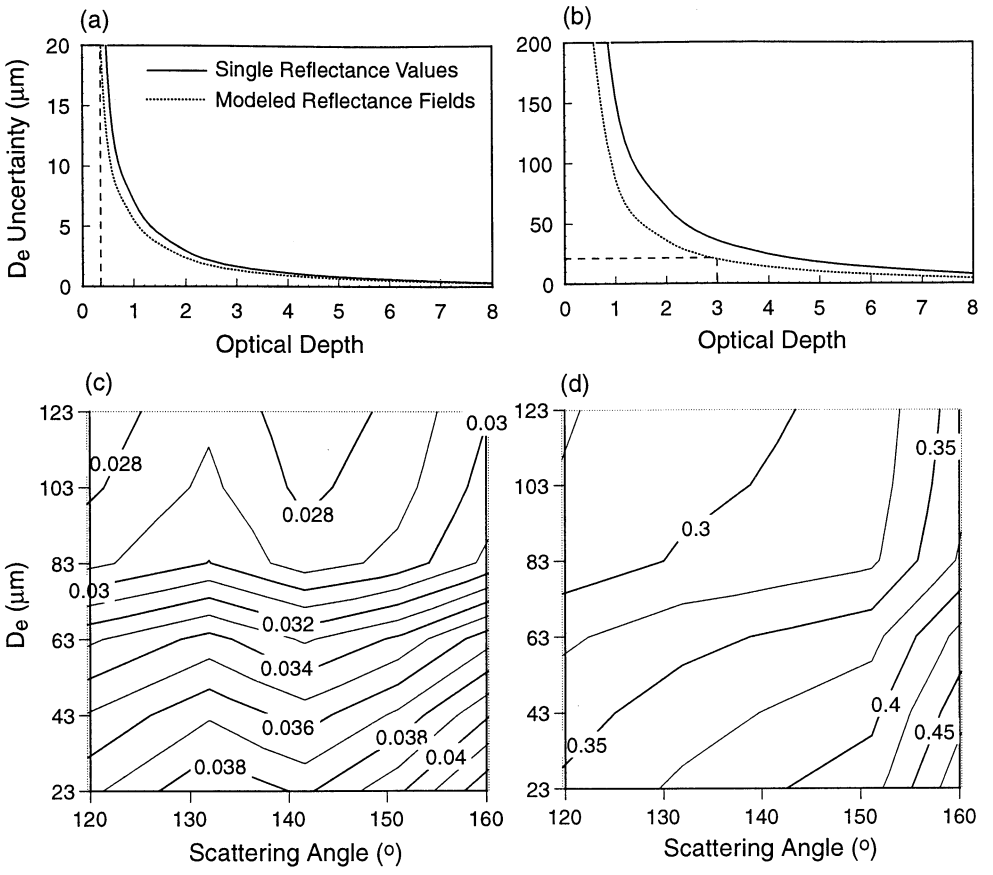

Figure 6. Uncertainties in the retrieved mean effective ice crystal size for the (a) ocean and (b) land scenes, shown as a function of the cirrus optical depth for corresponding forward calculations carried out using both the single values and the modeled fields of emerging cloud base reflectance. Uncertainties in the retrieved cirrus optical depth for the (c) ocean and (d) land scenes, shown as a function of the cirrus mean effective ice crystal size and the scattering angle for corresponding forward calculations carried out using the modeled fields of emerging cloud base reflectance.

for retrieval (dashed rectangle in Figure 1a) were computed using the sun/sensor geometry at a 1-km resolution, along with the aerosol optical depth and atmospheric profile that provided the best fit to the clear portion of the image. The resulting bidirectional reflectance fields (0.6, 1.6, and 2.2 μm) provide the cloud base reflectance (r_{cl}) values required to generate the lookup tables of the combined surface/atmosphere/cirrus reflectance using (7). These tables consist of theoretical bidirectional reflectance values for six mean effective ice crystal sizes (23 to 123 μm) and 10 cirrus optical depths (0.1 to 8). These values are subsequently interpolated using a bi-cubic spline technique to obtain a 1-μm resolution for the mean effective ice crystal size and a 0.1 resolution for the cirrus optical depth.

Retrievals of the optical depth and mean effective ice crystal size for thin cirrus identified in Figure 1a are conducted by using the lookup tables constructed from the preceding procedures. Results are shown in Plate 1. The scene averaged values of the retrieved cirrus optical depth and mean effective ice crystal size are 0.41 and 63.8 μm, respectively. Uncertainties involved in these results are assessed from the product of the sensitivity parameters defined in (9) and (10) and the averaged absolute spectral differences between the observed (R) and modeled (R_a) cloud-free reflectance fields defined by

$$\delta(\lambda) = \frac{1}{N}\sum_{i=1}^{N}\left|R_i(\lambda,\mu_0,\mu,\Delta\phi) - R_{a,i}(\lambda,\mu_0,\mu,\Delta\phi)\right|, \qquad (18)$$

Table 3. Parametric Coefficients for Equation (10)

	λ, μm	b_0, $\times 10^{-5}$	b_1, $\times 10^{-4}$	b_2, $\times 10^{-5}$
Ocean	1.6	-5.19	4.41	-1.66
	2.2	-3.77	4.03	-1.49
Land	1.6	-8.21	4.66	-1.89
	2.2	-6.92	4.41	-1.83

Table 4. Ecosystem Vegetation Classification Used in Land-Leaving Reflectance Calculations for April 20, 1996

Ecosystem	Vegetation Type
Northern mixed forest	60% Deciduous, 40% pine
Mixed forest	50% Deciduous, 50% pine
Evergreen needleleaf forest	100% Pine
Deciduous forest with pasture	60% Deciduous, 20% orchard, 20% annual
Grassland/woodland mosaic with cropland	40% Steppe, 40% coniferous, 20% plowed
Grassland (tall grass prairie)	50% Annual, 50% orchard
Grassland with cropland	100% Plowed
Grassland (warm season grasses)	60% Steppe, 40% plowed
Cropland with grassland	Cropland with grassland
Cropland with woodland	60% Plowed, 40% coniferous

where N is the number of pixels in the clear scene. The results are shown in Figures 6a and 6c. Based on these estimates, uncertainties associated with the retrievals shown in Plates 1a and 1b are calculated on a pixel-by-pixel basis, and are presented in Plates 1c and 1d. The scene-averaged retrieval results shown in Plate 1 have uncertainties associated with natural surface variability and anisotropy of ~0.03 and 16 μm for the retrieved cirrus optical depth and mean effective ice crystal size, respectively. Mean effective ice crystal size uncertainties are larger for thin cirrus. For a cirrus optical depth of ~0.1, mean effective ice crystal size uncertainties can reach 50 μm.

4.2. Land Surfaces

On April 20, 1996, MAS was flown over Kansas and Oklahoma during the SUCCESS field campaign. For the present study, track 6, shown in Figure 1b, which was collected between 1641 and 1653 UTC, was selected for its availability of a 45 km cloud free scene in the first portion of the track, as determined from concurrent Cloud Lidar System (CLS) data. Explicit computation (1 km resolution) of the reflectance as a function of the sun-sensor geometry for the 0.65 and 1.6 μm MAS channels was undertaken for the clear portion of the track using the method described in subsection 3.2. The ecosystems [*Loveland et al.*, 1995] associated with this track are shown in Plate 2. Unfortunately, due to the scarcity of *in situ* measurements, the input coefficients for the BRDF are available only for a few selective vegetation types. The combinations of vegetation and land surfaces used to represent the ecosystems in theoretical reflectance calculations are shown in Table 4. The mosaics of vegetation and soil types were determined from a trial and error process that provides the best fit between the computed and observed cloud-free reflectance values. In Figure 7, the observed reflectances are displayed for four scan lines at distances of 10 km, 20 km, 30 km, and 40 km from the start of the track, along with the computed reflectances and single values of the emerging reflectance obtained from a statistical analysis. It is clear that the complex visible and near-IR reflectance signals associated with natural variability and anisotropy of the land scene cannot be modeled using simple BRDFs and atmospheric correction calculations. Nevertheless, the preceding procedure significantly improves both the accuracy and precision of the emerging cloud base reflectance used in forward radiative transfer calculations in connection with the cirrus cloud retrieval. Scene averaged absolute values of the reflectance differences between the observed and modeled fields are 0.021 and 0.035 for the 0.65- and 1.6-μm channels, respectively. Corresponding uncertainty values associated with the retrieved cirrus parameters are shown in Figures 6b

Table 5. Comparison of the Mean Effective Ice Crystal Size (D_e) Uncertainties Using Single Spectral Values and Modeled Fields of the Emerging Cloud Base Reflectance in Forward Calculations

τ	D_e Uncertainty, μm (Single Values)	D_e Uncertainty, μm (BRDF Fields)	Relative Uncertainty Improvement, %
2	63.8	35.8	43.9
4	24.4	13.6	44.0
8	7.7	4.2	45.0

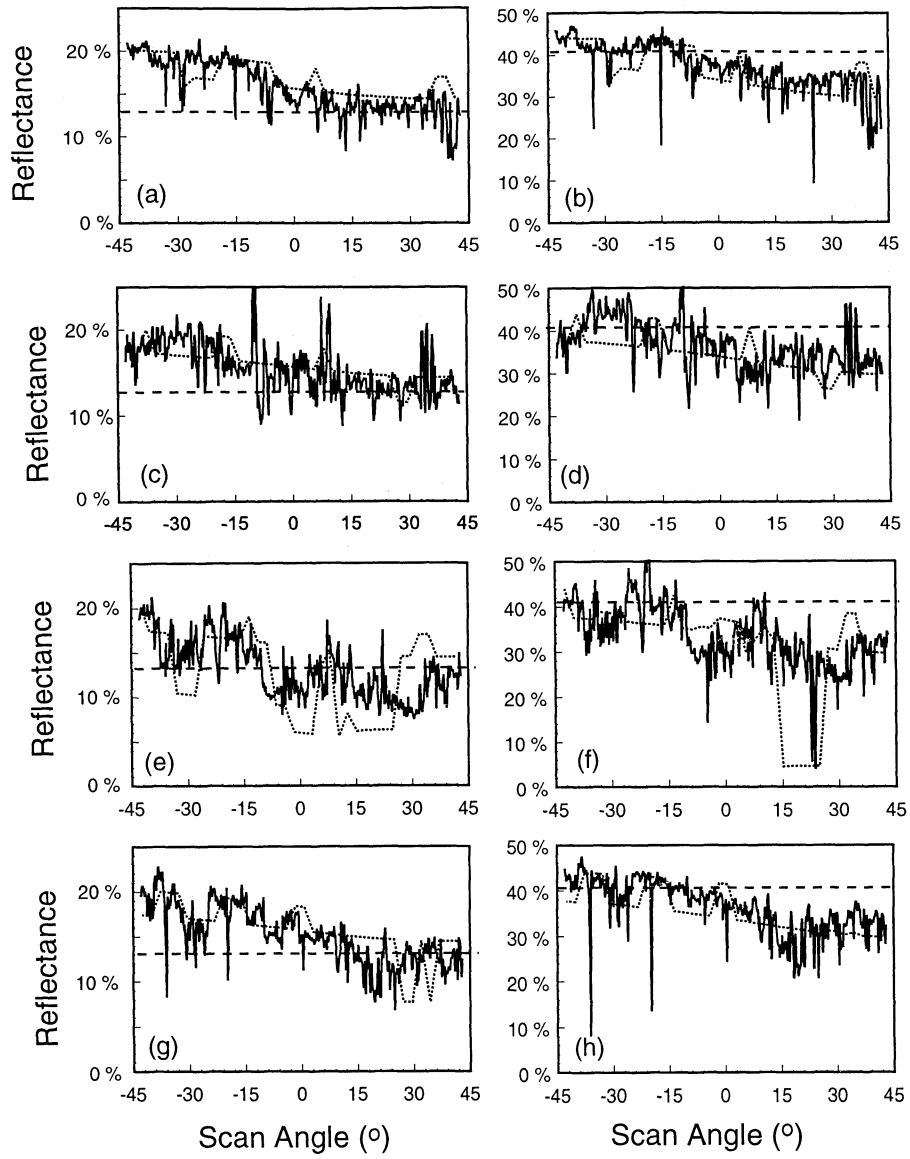

Figure 7. Observed (solid lines) and modeled (dotted lines) clear-sky reflectances for the 0.65 (a, c, e, and g) and 1.6 μm (b, d, f, and h) channels for four random scan lines at 10 km (g and h), 20 km (e and f), 30 km (c and d), and 40 km (a and b) along the track distance. Also shown for reference are the single values of reflectance obtained from a statistical analysis of the cloud-free pixels (dashed lines).

and 6d. From these results, it can be seen that uncertainties in the retrieval of cirrus optical depth and mean effective ice crystal size have been reduced by ~20 and 45%, respectively. Specific values of the mean effective ice crystal size uncertainties are presented in Table 5.

Optical depth retrieval for a cirrus observed on April 20, 1996, between 1633 and 1635 UTC was carried out using radiation lookup tables that incorporate the emerging cloud base reflectance determined from the theoretical model. Results are shown in Plate 3. The scene averaged cirrus optical depth is 0.71, thus implying large uncertainties in the retrieved mean effective ice crystal size in accordance with the results shown in Figure 6b. Uncertainty in the retrieved cirrus optical depth is illustrated by the discontinuities readily observed in Plate 3, which can be traced to surface variability and anisotropy effects.

5. Conclusions

On the basis of land and ocean scenes observed during SUCCESS, we demonstrate the importance of accurately incorporating the fields of emerging cloud base reflectance in the forward calculations of radiation tables for the remote sensing of thin cirrus. We then develop a means to simulate the cloud base reflectance based on the classification of land and ocean surfaces. Over the oceans the aerosol optical depth is determined from a simple microphysical model and is used to perform atmospheric correction of the emerging ocean surface bidirectional reflectance. Over the land surfaces we use a seasonal database of land cover and appropriate classification in terms of the vegetation and soil types to calculate the emerging bidirectional reflectance fields, based on a semiempirical theoretical model. This approach leads to

a significant reduction of the uncertainty associated with the surface variability and allows the retrieval of thin cirrus parameters with optical depths smaller than ~0.5 over oceans. It also reduces the uncertainties in the retrieved optical depth and mean effective ice crystal size for thin cirrus by ~20 and 45%, respectively, over complex land surfaces.

In spite of a significant improvement in the optical depth retrieval for thin cirrus, large uncertainties still exist in the determination of the mean effective ice crystal size, introduced by the reflection processes associated with complex land surfaces. It appears that additional information regarding the behavior of near-IR reflectances over various land surfaces would help to reduce the uncertainty in the ice crystal size retrieval.

Acknowledgments. This research was supported by NASA grants NAG5-6160 and NAG5-7738, and DOE Grant DE-FG03-00ER62904.

References

Arking, A., and J. D. Childs, Retrieval of cloud cover parameters from multispectral satellite images, *J. Clim. Appl. Meteorol., 24*, 322-333, 1985.

Cox, C., and W. Munk, Statistics of the sea surface from photographs of the Sun's glitter, *J. Mar. Res., 13*, 198-227, 1954.

Cox, C., and W. Munk, Some problems in optical oceanography, *J. Marine Res.*, 14, 63-78, 1955.

D'Almeida, G. A., P. Koepke, and E. P Shettle, *Atmospheric aerosols. Global Climatology and Radiative Characteristics*, 561 pp. A. Deepak, Hampton, Va., 1991.

Gordon, H. R., and M. Wang, Influence of oceanic whitecaps on atmospheric correction of ocean-color sensors, *Appl. Opt., 33*(33), 7754-7763, 1994.

Kimes, D. S., Dynamics of directional reflectance factor distribution for vegetation canopies, *Appl. Opt., 22*(9), 1364-1372, 1983.

Kimes, D. S., W. W. Newcomb, C. J. Tucker, I. S. Zonneveld, W. van Wijngaarden, J. de Leeuw, and G. F. Epema, Directional reflectance factor distributions for cover types of Northern Africa, *Remote Sens. Environ., 18*, 1-19, 1985.

Kimes, D. S., W. W. Newcomb, R. F. Nelson, and J. B. Schutt, Directional reflectance factor distributions of a hardwood and a pine forest canopy, *IEEE Trans. Geosci. Remote Sens., 24*(2), 281-293, 1986.

King, M. D., et al., Airborne scanning spectrometer for remote sensing of cloud, aerosol, water vapor and surface properties, *J. Atmos. Oceanic Technol., 13*, 777-794, 1996.

Koepke, P., Effective reflectance of oceanic whitecaps, *Appl. Opt., 23*(11), 1816-1824, 1984.

Liou, K. N., *An Introduction to Atmospheric Radiation,* 392 pp. Academic, San Diego, Calif., 1980.

Liou, K. N., Y. Takano, and P. Yang, Light scattering and radiative transfer in ice crystal clouds: Applications to climate research, in *Light Scattering by Nonspherical Particles*, edited by M. I. Mishchenko, J. W. Hovenier, and L. D. Travis, pp. 417-449, Academic, San Diego, Calif., 2000.

Loveland, T. R., J. W. Merchant, J. F. Brown, D. O. Ohlen, B. C. Reed, P. Olson, and J. Hutchinson, Seasonal land-cover of the United States, *Ann. of the Assoc. of Am. Geogr., 85*, 339-355, 1995.

Morel, A., and B. Gentilli, Diffuse reflectance of oceanic waters, II, Bidirectional aspects, *Appl. Opt., 32*, 6864-6879, 1993.

Morel, A., and P. Prieur, Analysis of variations in ocean color, *Limnol. Oceanogr., 22*, 709-722, 1977.

Nakajima, T., M. D. King, J. D. Spinhirne, and L. F. Radke, Determination of the optical thickness and effective particle radius of clouds from reflected solar radiation measurements, II, Marine stratocumulus observations, *J. Atmos. Sci.*, 48, 728-750, 1991.

Ou, S. C., K. N. Liou, W. M. Gooch, and Y. Takano, Remote sensing of cirrus cloud parameters using advanced very-high-resolution radiometer 3.7- and 10.9-μm channels, *Appl. Opt., 32*, 2171-2180, 1993.

Rolland, P., K. N. Liou, M. D. King, S. C. Tsay, and G. M. McFarquhar, Remote sensing of optical and microphysical properties of cirrus clouds using MODIS channels: Methodology and sensitivity to physical assumptions, *J. Geophys. Res., 105*, 11,721-11,738, 2000.

Roujean, J.-L., M. Leroy, and P.-Y. Deschamps, A bidirectional reflectance model of the Earth's surface for the correction of remote sensing data, *J. Geophys. Res., 97*, 20,455-20,468, 1992.

Stowe, L. L., A. M. Ignatov, and R. R. Singh, Development, validation, and potential enhancements to the second-generation operational aerosol product at the National Environmental Satellite, Data, and Information Service of the National Oceanic and Atmospheric Administration, *J. Geophys. Res., 102*, 16,923-16,934, 1997.

Strahler, A, and J. Townshend, in *MODIS land cover product algorithm theoretical basis doc.*, ATBD-MOD-version 4.1, NASA Goddard Space Flight Center, Greenbelt, Md., 1996.

Takano, Y., and K. N. Liou, Radiative transfer in cirrus clouds, II, Theory and computation of multiple scattering in an anisotropic medium, *J. Atmos. Sci., 46*, 20-36, 1989.

Vermote, E. F., D. Tanré, J. L. Deuzé, M. Herman, and J. J. Morcrette, Second Simulation of the Satellite Signal in the Solar Spectrum, 6S: an overview, *IEEE Trans. Geosci. Remote Sens., 35*, 675-686, 1997.

K. N. Liou and P. Rolland, Department of Atmospheric Sciences, University of California, Los Angeles, CA 90095-1565. (prolland@atmos.ucla.edu)

(Received September 26, 2000; revised February 7, 2001; accepted February 16, 2001.)